We are IntechOpen,
the world's leading publisher of
Open Access books
Built by scientists, for scientists

4,800
Open access books available

122,000
International authors and editors

135M
Downloads

Our authors are among the

154
Countries delivered to

TOP 1%
most cited scientists

12.2%
Contributors from top 500 universities

Interested in publishing with us?
Contact book.department@intechopen.com

Numbers displayed above are based on latest data collected.
For more information visit www.intechopen.com

Linde Type L Zeolite: A Privileged Porous Support to Develop Photoactive and Catalytic Nanomaterials

Leire Gartzia Rivero, Jorge Bañuelos, Kepa Bizkarra, Urko Izquierdo, Victoria Laura Barrio, Jose Francisco Cambra and Iñigo López Arbeloa

Additional information is available at the end of the chapter

Abstract

Among the wide assortment of zeolites based on aluminosilicates, Linde Type L (LTL) zeolite outstands as a support host owing to its porous framework and high adsorption surfaces. Thus, the incorporation of suitable guest molecules (fluorophores or metals) allows the development of photoactive and catalytic nanomaterials. In this chapter, we describe the design of materials based on LTL zeolite to achieve artificial antennae, inspired in the natural photosynthesis, and ecofriendly materials for the catalytic reforming of biogas. First, we describe the microwave-assisted synthesis of LTL zeolite with tunable size and morphology. Afterward, we test the energy transfer probability between the guest fluorophores into the LTL zeolite pores as the key process enabling the antenna behavior of this hybrid material with broadband absorption and tunable emission or predominant red fluorescence. Finally, we also test the behavior of LTL zeolite as a support material for the catalytic reforming of biogas. To this aim, suitable metals were impregnated onto LTL zeolite featuring different shapes and alkaline metal exchange. Activity tests indicated that disk- and cylinder-shaped hosts were the most active ones, especially when bimetallic (Rh-Ni) catalysts were prepared. However, the alkaline metal exchange was ineffective to increase the hydrogen yield.

Keywords: LTL zeolite, hydrothermal synthesis, nanomaterials, energy transfer, catalytic support, hydrogen

1. Introduction

Zeolites are crystalline silicates and aluminosilicates linked through oxygen atoms, producing well-defined three-dimensional structures with cavities and channels where water, cations,

and/or small molecules can allocate [1–5]. The term "zeolite" has its origin in the two Greek words *zeo* and *lithos*, literally meaning "boiling stone." The mineralogist Fredrik Cronstedt who observed that the heating of the material produced large amounts of steam water previously adsorbed by the pores coined this term in 1756 [6]. The zeolites are also known as molecular sieves and, albeit many of them occur naturally as minerals, most of these materials have been synthesized by the scientific community for different purposes in fundamental chemistry and technological fields. Nowadays, there are 191 types of zeolite frameworks registered and over 40 natural zeolite frameworks are known [7].

Likely, zeolites are the most widely used catalysts in the industry for oil refining, petrochemistry, and organic synthesis due to their high surface area and adsorption capacity, as well as their controllable adsorption properties [8]. Moreover, the possibility of designing frameworks *a la carte* with tunable porosity and chemical properties make them strong candidates for hosting different types of guests (such as ions, metals, and organic molecules) and for mass transport and/or occlusion [9].

Among the high diversity of natural and synthetic zeolites, Linde Type L (LTL) zeolite stands out owing to its appealing physicochemical and structural properties and high versatility [10]. LTL zeolite is a crystalline aluminosilicate of well-defined three-dimensional framework and a hexagonal symmetry (**Figure 1**). It is formed by corner sharing TO_4 tetrahedra (T being aluminum or silicon) leading to the arrangement of cancrinite cages and the final three-dimensional network. The presence of the trivalent aluminum infers an anionic character to the framework and charge-compensating cations are required to balance the charge of the tetrahedra. This is why the stoichiometry of LTL zeolite with monovalent charge compensating cations M^+ is $M_9[Al_9Si_{27}O_{72}] \cdot nH_2O$, where the number of water molecules n per unit cell equals 21 in fully hydrated materials and is about 16 at 20% relative air humidity. Its framework is characterized by uni-dimensional channels running along the c-axis of the crystal with a pore diameter suitable to host for many molecules of interest (7.1 Å), and hence, ideal to allocate organic fluorophores.
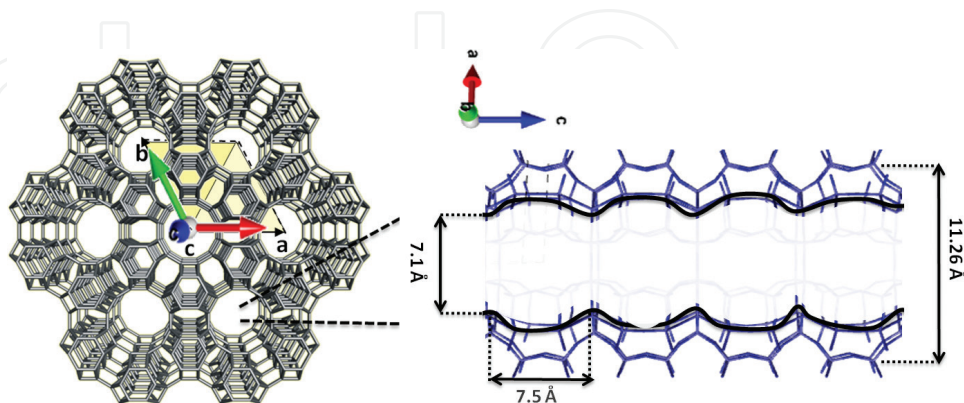

Figure 1. Top view of LTL zeolite framework, illustrating the hexagonal structure and the uni-dimensional pores. Side view of a channel that consist of 7.5 Å long unit cells with a van der Waals opening of 7.1 Å at the smallest and 11.26 Å at the widest place.
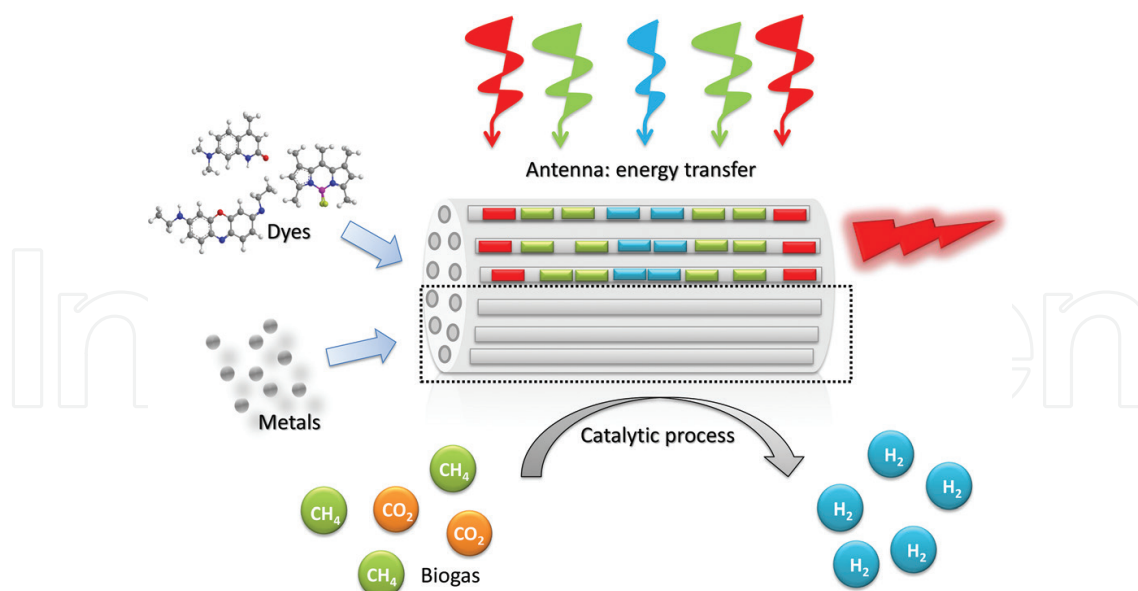
Figure 2. Schematic representation of the photoactive antenna and catalytic nanomaterials. Top: sequential insertion of three different dyes (absorbing and emitting in different ranges of the electromagnetic spectrum and undergoing energy transfer) into the LTL zeolite channels. Bottom: adsorption of metals onto the zeolitic surface to generate hydrogen from biogas by catalyzed reforming processes.

Over recent years, LTL zeolite has been successfully applied in a broad range of fields, including ion exchange and separation [11], catalytic processes [12], artificial antenna materials [13], photosensitizers in solar cells or light emitting diodes [14], luminescent solar concentrators [15], color changing media [16], microlasers [17], and in biomedicine [18].

In order to achieve competitive applications in advanced nanodevices is essential to provide high quality LTL zeolite crystals, which means, defined morphology, high crystallinity, and homogeneous size distribution of the particles. LTL zeolite is usually synthesized under hydrothermal conditions using conventional ovens. The crystal size and morphology are straightforwardly controlled by adjusting the starting gel composition (water content, alkalinity, or oxide proportion) as well as the heating conditions (heating rate and/or temperature). LTL zeolites with sizes ranging from nanometers to micrometers and disc-shaped or barrel-like morphologies have already been reported [19, 20].

Herein, we present a novel synthetic approach relied on the use of microwave-assisted heating for the production of high quality LTL zeolite crystals with tunable size and morphology. These inorganic crystals will then act as scaffolds for antenna systems (inspired in biosynthetic organisms), as well as environmentally friendly catalytic supports for energetic applications (metal-catalyzed hydrogen production from biogas reforming) (**Figure 2**). Indeed, the pore diameter of the host fits well to allocate organic fluorophores inside, whereas the constrained environment of the channel arranges hierarchically the chromophores, boosting the energy transfer, and hence, the antenna effect. Besides, the high adsorption capability of this support material, owing to its large available surface area, enables the efficient absorption of high amount of metals, thereby, enhancing the catalytic activity.

2. LTL zeolite: microwave-assisted hydrothermal synthesis

Microwave heating is an emerging technique in modern organic synthesis and in the production of nanoparticles and nanostructures. It usually affords an improvement in the yield and reproducibility of the synthetic processes, reducing the energetic costs, and favoring a friendlier environmental methodology [21, 22]. The main characteristics of microwave-assisted heating rely on the accurate control of the temperature, which ensures homogeneous distribution of the heat, preventing temperature gradients within the oven and samples. Therefore, the heating process is more efficient, side reactions are avoided in great extent, and as a consequence, reaction times are reduced notably.

This section is focused on describing the hydrothermal synthesis of LTL zeolite by extrapolating the optimal conditions referred in previous reports for conventional ovens and applied them to microwave heating [19]. One of the main aims is to improve the quality of the crystals and decrease reaction times, which otherwise takes several days and implies higher energetic costs. In this regard, we have studied the effect of reaction conditions (heating rate, time, temperature, and static/dynamic conditions) on the size, morphology and chemical properties of the resulting crystals. Thus, LTL zeolite crystals with size ranging from nanometers (15 nm) to micrometers (3 μm), and shape varying from disc or coin to barrel have been synthesized by tuning the gel composition and the aforementioned reaction conditions.

The herein used hydrothermal synthetic procedure is described in **Figure 3**. The general protocol consists on mixing two aqueous suspensions, one containing the silica source and the other composed by the aluminum source, in a basic environment, leading to a milky gel phase. Afterward, the gel is heated (at reaction temperatures usually higher than 100°C) in a sealed high-pressure polytetrafluoroethylene (PTFE) vessel for a certain time period (optimal for each kind of zeolite). The size and morphology of the crystals can be modulated by changing the source of reactants, composition of the gel (alkalinity, water content, SiO_2/Al_2O_3, among others) reaction time, temperature, and aging time of the gel [23]. To this aim and, starting from a fixed gel composition optimized for each kind of zeolite, we focused on modifying the reaction conditions and gel pre-treatment for a fine-tuning of the size and morphology of the crystals. For all types of zeolites the microwave-assisted heating reduced the synthesis times up to 90% (days to hours) compared to the one afforded by conventional ovens [19, 23]. Moreover, the precise control of the temperature and the homogeneous heating during the nucleation process in the microwave oven are reflected in a narrower size distribution of the particles and higher degree of crystallinity. Therefore, LTL zeolite crystals of different sizes and morphologies, and improved quality, can be attained in few hours, with the consequent time and energetic savings. The properties of these zeolites were further studied and classified to best fit different kind of applications.

2.1. LTL zeolite nanocrystals

The small size of these zeolites (15–50 nm) is suitable to allocate guests deep inside the pores thanks to the favored diffusion within the pores [23]. Furthermore, its large external surface makes them optimal supports for adsorption processes, e.g., adsorption of metal particles for catalytic processes [12].
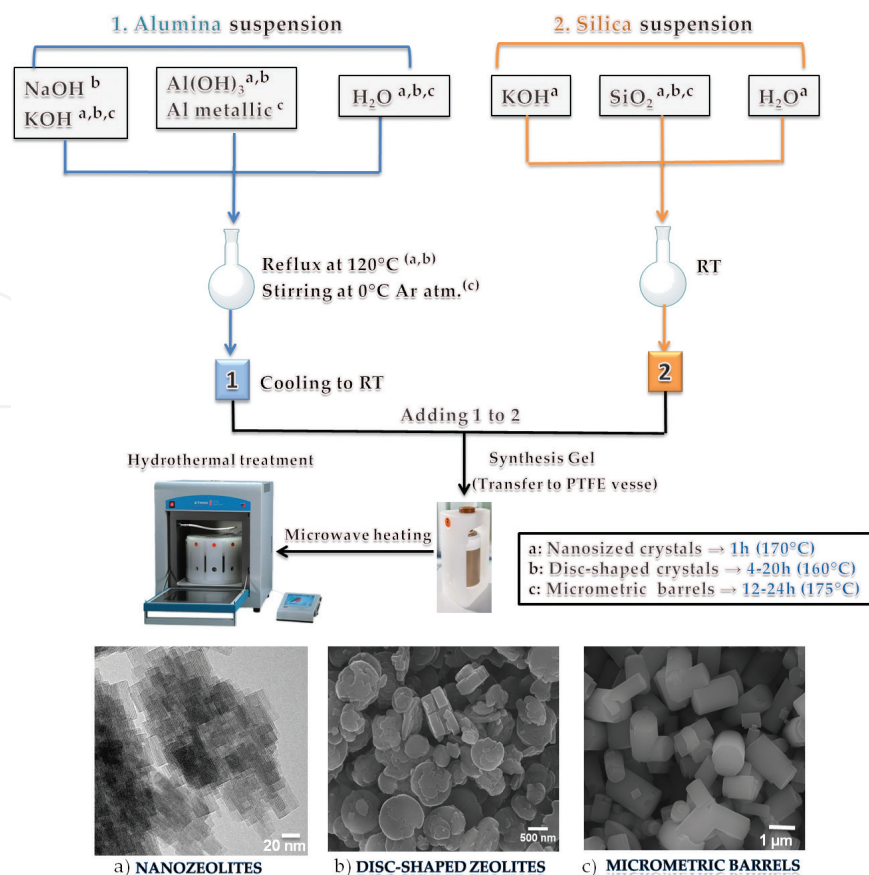
Figure 3. Scheme of the hydrothermal synthesis route for (a) nanosized, (b) disk-shaped, and (c) micrometric barrel-shaped LTL crystals and its respective morphologies analyzed by (a) transmission electron microscopy (TEM) and (b) and (c) scanning electron images (SEM) micrographs.

The synthesis procedure is described in **Figure 3** (route a) and the oxide molar ratio in the gel was fixed at 9.34 K_2O:1.00 Al_2O_3:20.20 SiO_2:412.84 H_2O. After heating the gel at 170°C under pressure for 1 h nanocrystals sizes were successfully obtained, where the size can be tuned from 15 to 50 nm by adjusting the synthesis conditions (gel ripening, static/dynamic conditions, or different silica sources). These nanosized LTL zeolites were subsequently used in energetic and photonic applications, such as catalytic supports for biogas reforming and fabrication of artificial antenna systems, respectively.

2.2. Disk-shaped LTL zeolite crystals

Disk-shaped crystals, characterized for having a low aspect ratio (length/diameter), were also synthesized in which their thickness and diameters were modified in a controlled way. This morphology is desirable to ease their coupling with external devices (e.g., to produce uniform and well-organized monolayers or membranes [10]), and to afford high number of uni-dimensional pores with short diffusion path lengths (around 100,000 channels in a crystal with diameter of 600 nm [24]).

The synthetic procedure is presented in the route b of **Figure 3**, starting in all cases from a fixed gel composition of 5.40 K_2O:5.50 Na_2O:1.00 Al_2O_3:30.00 SiO_2:416.08 H_2O oxides molar ratio and heating at 160°C. The variation of factors controlling the growing of the crystal, such

as the heating rate and the reaction time, allows the production of crystals with lengths ranging from 130 to 200 nm, and diameters spanning from 600 to 1200 nm.

2.3. Micrometric LTL zeolite barrels

The synthesis of large LTL zeolite crystals (from 1500 to 3000 nm length) with well-defined morphology and high aspect ratio (barrels-like microcrystals) has proven to be useful in the analysis of the distribution, orientation, and interaction of guest molecules by time- and space-resolved fluorescence measurements, such as fluorescence confocal microscopy at single-particle level [25].

The synthetic procedure is presented in the route c of **Figure 3**, starting in all cases from a fixed gel composition of 2.21 K_2O: 1.00 Al_2O_3:9.00 SiO_2:164.60 H_2O oxides molar ratio in the mixture and heating at 175°C.

To avoid undesirable process (mainly with organic dyes) owing to the high acidity of the channels, these synthesized zeolites were cation-exchanged with cesium or sodium.

3. Photoactive antenna materials

3.1. Dye-doped LTL zeolite

This section describes the development of photoactive nanomaterials based on the supramolecular organization of luminescent molecules into the channels of LTL zeolite. Taking inspiration from nature we will focus on one of the most sophisticated and vital processes in the earth, the photosynthesis, to develop a new generation of fluorescent nanomaterials. Using the *modus operandi* of the natural antenna systems present in photosynthetic organisms as a reference point, the main goal focused on the design and construction of artificial antenna systems able to mimic the functions and mechanism of these natural entities.

Many scientists all over the world are active participants in the challenge of developing artificial photoactive nanomaterials able to imitate the perfection and high efficiency of the mechanisms present in nature [26–28]. As a significant example, the photosynthetic organism present in plants appear as the most sophisticated solar energy storage systems in nature due to their unique ability to harvest solar radiation and transform it into chemical energy. The antenna systems, composed by few hundred of chlorophyll molecules are embedded in a protein environment (which keeps the photoactive moieties well arranged), are the responsible for absorbing the light and transfer the excitation energy to a specific reaction center [29]. Therefore, one of the main requirements for the proper operation of an artificial antenna system is the ability to harvest and transport the light to an acceptor moiety with the desired energy (**Figure 4**). The excitation energy transfer (EET) is a key factor ruling the effectiveness of the process. A careful understanding of the parameters controlling this phenomenon is mandatory, such as spectral overlap, ratio of donors and acceptors, interchromophoric distances, and relative orientations. The precise control of these variables enables the development of high-quality artificial antenna systems with potential applications in photonics,
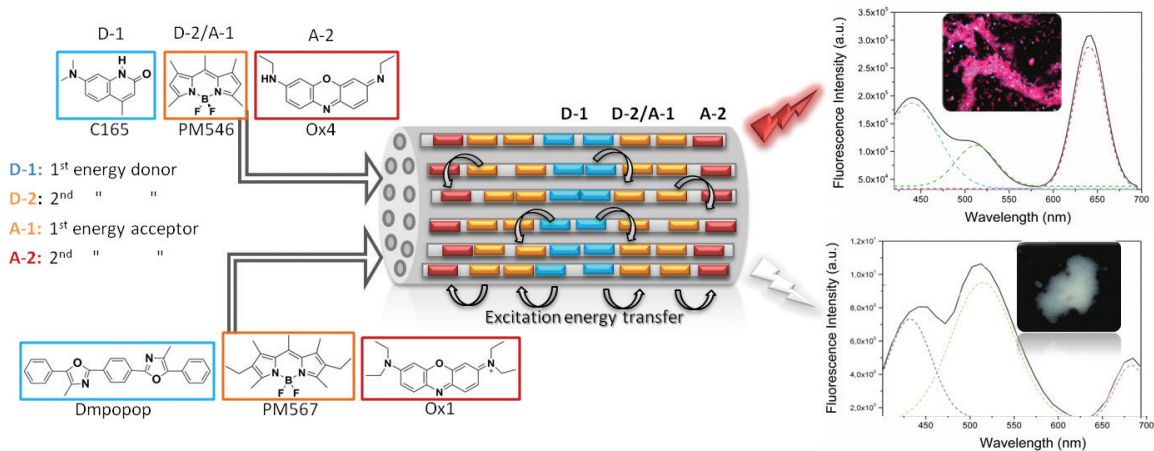
Figure 4. Schematic representation of the designed antenna material by means of the sequential insertion of three different dyes into LTL zeolite channels. The molecular structures of the two tested antenna systems using carbostyril (C165) and an oxazole (Dmpopop) as the blue-emitting energy donors, BODIPYs (PM546 and PM567) for the green-yellow region, and oxazines (Ox4 and Ox1) as red emitting final acceptors are also enclosed. The corresponding fluorescence spectra (upon selective excitation at the blue donor, 350 nm) and image (by fluorescence microscope) for each dye combination are also included. In all cases, the dye amount was the 10% of the available adsorption sites and the donor/acceptor ratio was 1:1:1.

optical coding, biosensing, catalysis, photosynthesis, logic devices, and theranostics, just to highlight some of them [30–32].

In our particular case, the strategy to develop competitive artificial antenna systems is based on the design of photoactive organic-inorganic hybrid materials. The protein matrix present in natural systems has been replaced by the LTL zeolitic host of nanometric dimensions, which apart from protecting the dyes, provides a constrained environment that induces a high degree of supramolecular organization. Furthermore, regarding the photoactive moiety, responsible for interacting with the light, the chlorophyll molecules have been replaced by small enough fluorescent molecules working in different regions of the electromagnetic spectrum (to ensure broadband absorption across the whole visible spectral region) and susceptible of promoting efficient EET processes. The energy transfer takes place via dipole-dipole coupling, better known as the through-space Förster mechanism (FRET), where one of the main requirements is the proper spectral overlap between the emission spectrum of the donor and the absorption spectrum of the acceptor. Therefore, by properly choosing the dyes to be encapsulated and controlling the spectral overlap of the combined dyes, the FRET efficiency can be finely tuned, and hence, the output emission light of the photoactive material will be modulated accordingly (**Figure 4**) [13, 33].

Here we present two antenna systems built by the sequential insertion of three different dyes into the pores of the LTL zeolite (**Figure 4**). As energy donors, oxazole (Dmpopop) and carbostyril (C165) dyes have been considered in the UV-blue region, whereas in the green-yellow part, BODIPYs (PM546 and P567) have been selected as first acceptors and succeeding energy donors. Finally, red-emitting oxazines (Ox1 and Ox4) where chosen as final energy acceptors. The UV-blue donors are placed in the center of the crystal, flanked by the green-yellow dyes, and with the red acceptors localized at the edges of the LTL zeolite crystal. In both antenna systems, the light is efficiently harvested over a broad spectral region and after selective excitation at the UV region, where only the first energy donors absorbs (C165 and Dmpopop,

respectively), its own emission is recorded but followed by that from the BODIPYs (PM546 and PM567) and the last energy acceptors (Ox4 and Ox1) (**Figure 4**).

However, there is a notorious difference in the energy output of each antenna system due to the different FRET process efficiency between the encapsulated dyes. The higher degree of spectral overlap in the antenna, composed by C165-PM546-Ox4 dyes, leaded to an efficient transformation of the harvested light into red emission (**Figure 4**). On the other hand, the less pronounced spectral overlap in the antenna, composed by Dmpopop-PM567-Ox1, decreased the FRET efficiency leading to the simultaneous detection of the emission from the three different chromophores with similar intensity. The sum of all these emissions covering the whole visible spectrum leads to white-light emission in which the energy output can be finely modulated over a broad region just using suitable filters (**Figure 4**). Therefore, by controlling the efficiency of the FRET hops, via the optimization of the magnitude of spectral overlap between the luminescent molecules inside de zeolitic channels, a fine modulation of the outcoming light energy can be reached, and hence either red-light or white-light emitting photoactive materials can be achieved.

3.2. External functionalization of LTL zeolite

In order to improve the degree of supramolecular organization, we tested a strategy based on the external functionalization of the channel entrances of LTL zeolite with tailor-made molecules (stopcock) via covalent linkage of such fluorophore (**Figure 5**) [13, 14]. These stopcock molecules grafted at the pores plug the channels to avoid the leakage of the guest molecules adsorbed inside and connect the inner space of the zeolite with the outside thanks to FRET processes, making the coupling of the material with other external devices straightforward.

The rational design of the stopcock molecule appears as key factor to ensure the suitable performance of it. On one hand, it needs to be small enough to diffuse into the pores and have the required functionalization to be covalently grafted at the channel entrances by reaction with free silanol groups (**Figure 5**). On the other hand, the emission should be placed at the red-edge of the visible spectral region to act as proper acceptor of the light harvested into the zeolitic channels. In this regard, we have designed a molecule made up of a label (triethoxysilane), a spacer and a head moiety (the fluorophore itself), taking BODIPY dyes as scaffold, owing to its excellent photophysical signatures and chemical versatility of its dipyrrin core subject to a plethora of organic reactions [34], and modified its backbone accordingly to fulfill the above mentioned perquisites. The next step consisted on the construction of the antenna system by its combination with a suitable energy donor; in this case, the above tested oxazole (Dmpopop), since it shows a broad absorption band in the UV-blue region and its emission overlaps well with the absorption band of the BODIPY-based stopcock. Therefore, the Dmpopop donor has been first inserted in the channels and right after the entrances were plugged with the silylated BODIPY. The selective excitation of the donor leads to a predominant red fluorescence from the stopcock centered at 610 nm (**Figure 5**), proving the ongoing FRET process from the inside to the outside of the crystal along the channel direction. Thus, the stopcock molecules enable the communication between the guest molecules encapsulated inside the pores with external materials or molecules outside. Besides, this closure molecule prevents small molecules like water or oxygen (fluorescence quenchers) from diffusing into the inner space of the crystals.
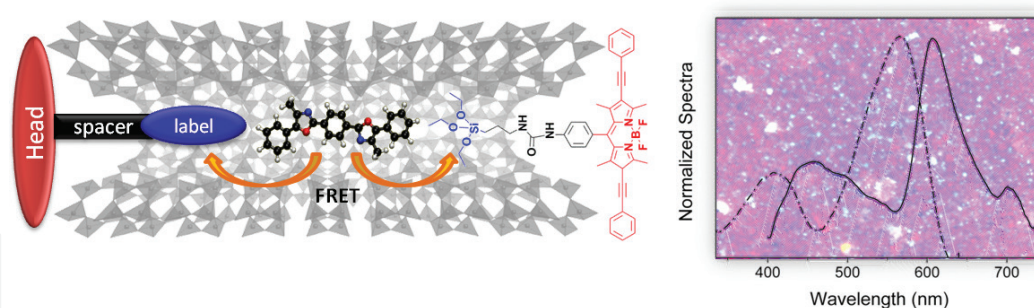
Figure 5. Schematic view of LTL zeolite channel doped with Dmpopop as energy donor (center), and the BODIPY-stopcock attached to the channel entrances as energy acceptor. The molecular structure of the stopcock and a scheme representing its three main components are shown in different colors. The corresponding normalized excitation (emission monitored at 600 nm, dashed line) and emission (excited at 350 nm, solid line) spectra, as well as the fluorescence microscopy image are also depicted.

4. LTL zeolite for hydrogen production through methane reforming processes

Catalyst supports play a key role in the process as it provides properties such as thermal stability, surface area, acidity, or the capacity of maintaining the metal dispersion during the reaction process. Those properties can be key factor for a catalyst to stand out from the existing ones [35]. For methane reforming processes, alumina supports are commonly used as they fit the mentioned properties [35–38]. Nevertheless, those properties are also present on zeolites. Accordingly, some zeolites were tested as support for methane reforming processes, in which, the influence of the nature of the zeolite support on the catalyst performance was analyzed [39, 40].

LTL zeolite has been used as catalyst support for methane reforming for hydrogen production, because hydrogen is considered the fuel of the future. For that purpose, LTL zeolite featuring different shapes (disc (DL), cylinders (CL), and nanocrystals (NL)), sizes (for the CL zeolites, between 1 and 3 μm and 30–60 nm) and alkaline metal (for the DL zeolites, with Cs, Na, or without them) exchange were used as catalyst support. Those supports were impregnated with nickel (13 wt.%) or co-impregnated with nickel and rhodium (13 and 1 wt.%, respectively) in order to prepare the corresponding monometallic or bimetallic catalysts, following the wet impregnation procedure [12, 23].

Nickel is a metal widely used for reforming processes because of its availability and relatively low price. On the other hand, although noble metals are more expensive than non-noble metals, it has been reported that the addition of small amounts of a noble metal to a non-noble metal catalyst increases the activity and dispersion of the non-noble metal due to the spill-over effect [41]. Therefore, a low amount of rhodium was incorporated to prepare bimetallic catalysts.

4.1. Chemical composition

The content of the metal incorporated into the zeolite supports was determined by Inductively Coupled Plasma-Atomic Emission Spectroscopy (ICP-AES) model 2000 DV (Perkin Elmer)

instrument. The composition, summarized in **Table 1**, indicates that the measured values were close to the nominal ones.

4.2. Textural properties

The textural properties of the LTL zeolite supported catalysts were determined by means of N_2 adsorption-desorption isotherms obtained at 77 K using an Autosorb-1C-TCD. The measured textural property values were not only affected by metal incorporation, but also by the calcination carried out on the catalyst preparation procedure.

The calcinations at 1073 K for 4 h before the metal impregnation produced an important decrease in the textural properties of the LTL zeolite, as shown in **Table 2**. As it could be expected, those values were further reduced when the metal impregnation and catalysts calcinations were carried out, as shown in **Tables 2** and **3**.

Due to the low amount of noble metal impregnated on the zeolites (1 wt.%), differences on the textural properties for monometallic and bimetallic catalysts (**Table 2**) were only observed for CL (30–60 nm) supported catalysts. The bimetallic catalyst presented a lower SSA value, in accordance to its higher pore volume and much higher PD, probably due to a higher coverage

Support	Rh	Ni	Catalyst	Rh	Ni
Ni/DL	—	11.1	Rh-Ni/DL	0.9	12.9
Rh-Ni/DL	0.9	12.4	Rh-Ni/DLCs	0.8	12.4
Ni/CL (1–3 μm)	—	12.7	Rh-Ni/DLNa	0.8	11.6
Rh-Ni/CL (1–3 μm)	1.0	14.0	Rh-Ni/NL	0.9	13.8
Ni/CL (30–60 nm)	—	11.9	Rh-Ni/NLCs	0.8	13.3
Rh-Ni/CL (30–60 nm)	1.1	13.2	Rh-Ni/NLNa	0.9	11.6

Table 1. Chemical compositions for catalysts prepared with LTL zeolite expressed as wt.% [12, 23].

Support	SSA (m²/g)	PV (cm³/g)	PD (Å)	Catalyst	SSA (m²/g)	PV (cm³/g)	PD (Å)
DL (F)	258	0.04	14	Ni/DL	40	0.10	54
DL (C)	134	0.06	17	Rh-Ni/DL	42	0.12	63
CL (1–3 μm) (F)	260	0.05	13	Ni/CL (1–3 μm)	23	0.05	55
CL (1–3 μm) (C)	152	0.04	13	Rh-Ni/CL (1–3 μm)	26	0.07	58
CL (30–60 nm) (F)	419	0.90	54	Ni/CL (30–60 nm)	95	0.45	96
CL (30–60 nm) (C)	335	0.93	67	Rh-Ni/CL (30–60 nm)	64	0.63	198

Table 2. Textural properties, specific surface area (SSA), average pore volume (PV) and average pore diameter (PD), of fresh (F) and calcined (C) LTL zeolite and their corresponding monometallic and bimetallic catalysts [12].

of the low size pores. Nevertheless, both CL (30–60 nm) supported catalysts presented the highest BET areas.

It is worth mentioning that in the cases of the metal impregnation on DLCs and DLNa catalysts, the measured BET area increased (**Table 3**). That happened due to the creation of new area with the metallic particles, as the original LTL zeolite surface area was low.

4.3. Temperature programmed reduction (TPR)

Catalysts reducibility was evaluated by temperature programmed reduction (TPR) using an Autosorb-1C-TCD device. The obtained reduction profiles are summarized in **Figure 6**. The profiles in the left side of **Figure 6** show that for bimetallic catalysts the reduction processes start at lower temperatures than their corresponding monometallic catalysts, probably due to the spill-over effect [12].

Support	SSA (m²/g)	PV (cm³/g)	PD (Å)	SSA (m²/g)	PV (cm³/g)	PD (Å)	SSA (m²/g)
DL	59	0.07	30	Rh-Ni/DL	38	0.13	72
DLCs	13	0.08	122	Rh-Ni/DLCs	17	0.13	155
DLNa	1	<0.01	264	Rh-Ni/DLNa	3	<0.01	251
NL	210	0.79	79	Rh-Ni/NL	68	0.19	59
NLCs	96	0.65	136	Rh-Ni/NLCs	37	0.15	85
NLNa	144	0.74	106	Rh-Ni/NLNa	43	0.17	77

Table 3. Textural properties, specific surface area (SSA), average pore volume (PV) and average pore diameter (PD), of LTL zeolite and their corresponding bimetallic catalysts [12].
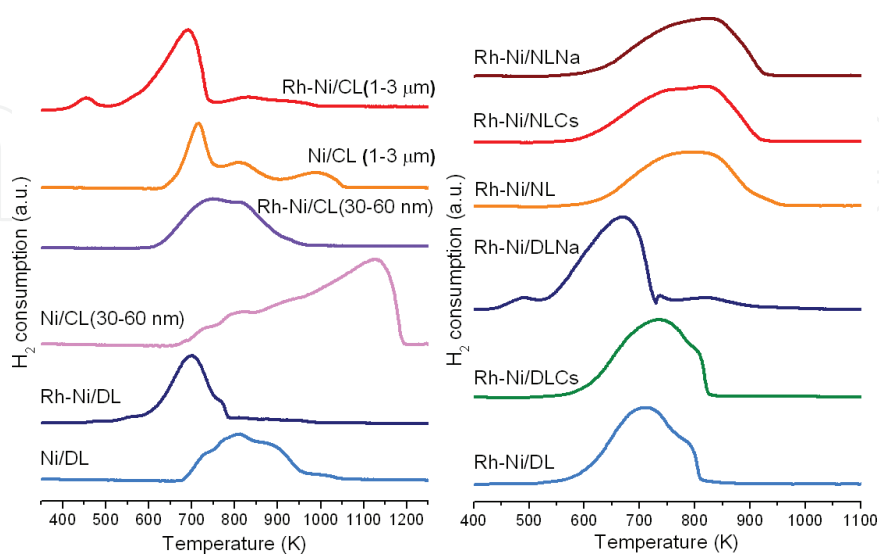

Figure 6. TPR profiles for zeolite L supported catalysts, modified from [12, 23].

Both, CL (1–3 μm) supported catalysts and Rh-Ni/DL catalyst, presented the main reduction peak around 700 K due to the reduction of NiO with low interaction with the support [42]. Ni/CL (1–3 μm) catalyst presented other two small peaks at 820 and 1000 K originated by the reduction of NiO particles with high interaction with support and Ni species located on the hexagonal prism, respectively [43]. Bimetallic CL (1–3 μm) and DL supported catalysts did not show those two reduction peaks, probably because they produced a more intense peak attributed to the NiO with low interaction with the surface. However, they presented a low peak and a shoulder at temperatures around 820 K, which could also be produced by the reduction NiO with high interaction with the surface. Similar profiles were produced for Rh-Ni/DL with and without alkali metal exchanged.

Ni/DL, Rh-Ni/CL (30–60 nm), and NL supported catalysts also presented similar profiles. On them, the hydrogen consumption peaks that took place around 700–750 K were produced by the reduction of NiO species [42, 44]. The reductions that took place at higher temperatures (~800 K) could be assigned to NiO particles with stronger interaction with support [43].

Among the studied catalysts, Ni/CL (30–60 nm) catalyst produced its main reduction peaks at the highest temperature (1150 K) because of the reduction of non-stoichiometric and stoichiometric Ni-spinels [45].

Rhodium reduction peaks were only detected for Rh-Ni/CL (1–3 μm) and Rh-Ni/DLNa catalysts at temperatures around 450 K [46]. Therefore, rhodium is probably stronger interacting with support in the other bimetallic catalysts, and thus, its reduction peak could be covered by more intense H_2 consumptions produced by Ni species.

4.4. X-ray diffraction (XRD)

Before activity tests, catalysts were also analyzed by X-ray diffraction (XRD) using a Philips X'PERT PRO automatic diffractometer operating at 40 kV and 40 mA, in theta-theta configuration, secondary monochromator with Cu Kα radiation (λ = 1.5418 Å) and a PIXcel solid state detector. Diffraction patterns are shown in **Figure 7**. In the left side of the figure, the XRD patterns of fresh calcined monometallic and bimetallic catalysts are shown, while on the right side the patterns of other reduced zeolite L with and without alkali modification supported catalysts are collected.

All the patterns of the LTL zeolite supported catalysts showed characteristic peaks of the LTL zeolite at 2 theta (θ) degrees from 10 to 42. Nevertheless, the intensity of the peaks is lower for the reduced catalysts. The loss of the intensity could be caused by the loss of the crystallinity happened during the reduction treatment. Accordingly, for some of the reduced catalysts, there is only a broad peak in the range in which LTL zeolite peaks should be placed, i.e., Rh-Ni/DLNa, Rh-Ni/NLCs, or Rh-Ni/NLNa catalysts.

Apart from the diffraction peaks attributed to the LTL zeolite structure, fresh calcined catalysts produced diffraction peaks attributed to NiO (Powder Diffraction File (PDF): 01-044-1159) at 43 and 63 2 theta degrees.

On the other hand, the XRD analyses for reduced LTL zeolite supported catalysts presented metallic nickel peaks at around 44 and 53 2 theta degrees (PDF: 01-087-0712). For these catalysts, peaks corresponding to nickel oxides were not observed.
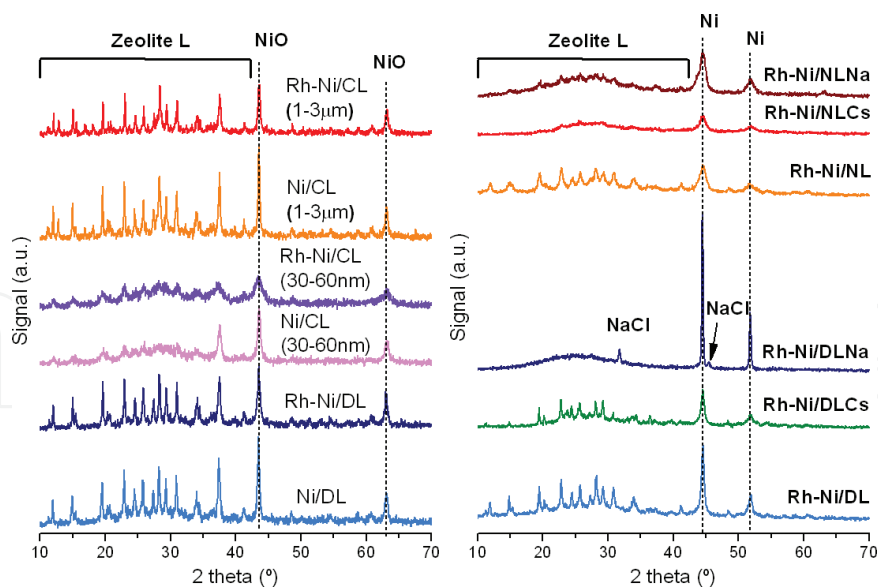
Figure 7. XRD patterns of zeolite L supported catalysts, modified from [12, 23].

The application of Scherrer equation on the most intense nickel diffraction peaks (2θ = 43 and 2θ = 44 for nickel oxide and metallic nickel, respectively) showed that, in general, bimetallic catalysts presented smaller NiO crystallite sizes (~30 nm) than their homologous monometallic catalysts (~60 nm), meaning that the active metal could be better dispersed in the bimetallic samples. The DL supported catalysts were the exception, as both monometallic and bimetallic catalyst containing NiO crystallites around 30 nm.

XRD analyses did not provide any diffraction peak attributed to rhodium (neither metallic nor oxide). Thus, rhodium particles smaller than the detection limit of the equipment (<4 nm) could be present on the catalysts, as the presence of rhodium on the catalysts was assured by ICP-AES.

For the LTL zeolite with and without alkali metal modification (Cs or Na) the estimated crystallite sizes were from 10 to 25 nm. In this case, Rh-Ni/DLNa catalyst was the exception and presented nickel crystals around 100 nm, as it can be observed in the TEM images (**Figure 8**) acquired on a Philips CM 200 transmission electron microscope at an acceleration voltage of 200 kV with a LaB$_6$ filament. The high crystallite size could be related with the low surface area and the consequent higher nickel agglomeration on the surface of the catalyst.

4.5. X-ray photoelectron spectroscopy (XPS)

The catalysts prepared with DL and NL with and without alkali modification were also reduced and analyzed by X-ray photoelectron spectroscopy (XPS) in order to compare surface (XPS) and bulk (ICP-AES) nickel and rhodium abundances. Results are summarized in **Table 4**. For that purpose, a VG Escalab 200R spectrometer equipped with a hemispherical electron analyzer and an Al Kα1 (hν = 1486.6 eV) 120 W X-ray source was used.

Both metals, Ni and Rh, were preferentially located on the external surface of the catalysts as indicated by the Ni/zeolite and Rh/zeolite ratios which were higher for the XPS than for
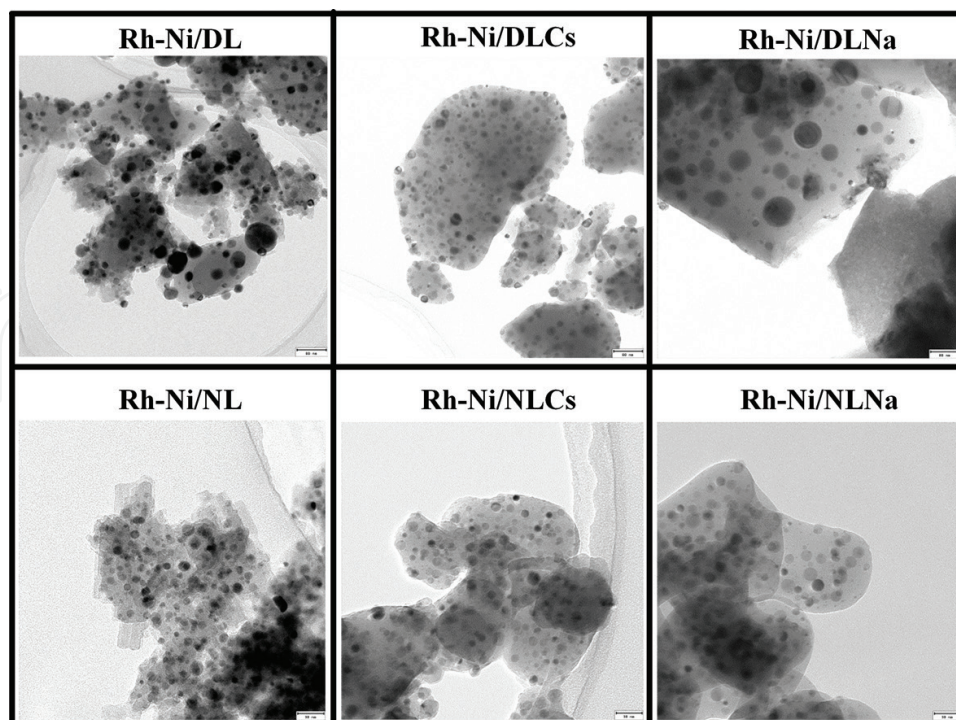
Figure 8. TEM images of the calcined catalysts. Scale size for DL and NL of 80 and 30 nm, respectively. Modified from [12].

Catalyst	Atomic ratios XPS/ICP	
	Ni/zeolite L	Rh/zeolite L
Rh-Ni/DL	3.10/0.22	0.89/0.01
Rh-Ni/DLCs	5.61/0.24	1.06/0.01
Rh-Ni/DLNa	5.17/0.25	−/0.01
Rh-Ni/NL	0.47/0.22	0.29/0.01
Rh-Ni/NLCs	2.02/0.26	0.44/0.01
Rh-Ni/NLNa	1.81/0.27	−/0.01
Modified from [23].		

Table 4. Comparison of the surface atomic ratios measured by XPS and the bulk atomic ratios measured by ICP.

the ICP-AES. The difference between the high XPS and lower ICP-AES ratios were more significant for DL with and without Cs and Na modification supported catalysts, because they presented the lowest SSA values. On the other hand, for DL and NL supported catalysts, a similar trend was observed; the lowest metallic content on the external surface was measured to the unmodified support, while highest values were measured for the Cs containing catalysts. Therefore, the presence of Cs and Na hinders the metal incorporation into the pores [23].

4.6. Catalytic activity

The catalytic activities of the monometallic and bimetallic catalysts supported on DL, CL (30–60 nm) and CL (1–3 μm) were evaluated for 90 min at 1073 K and atmospheric pressure under different biogas reforming conditions, summarized in **Table 5**.

A ¼ inch 316 L stainless steel fixed bed reactor was used for the experiments. The catalytic bed was composed of 0.34 g of catalyst (0.42 < particle diameter (dP) < 0.50 mm) mixed with 1.53 g of inert CSi (0.50 < dP < 1.0 mm). The catalytic bed was placed in the middle of the length of the reactor and kept in place by filling the rest of the reactor with inert CSi (1.0 < dp < 3.0 mm).

The reactor was placed in a Microactivity Reference bench-scale plant (PID Eng&Tech) to perform the activity experiments. Biogas ($CH_4 + CO_2$), N_2 and O_2 were fed by electronic controllers, while deionized water was injected using an HPLC-Gilson water pump. Catalysts were reduced at 1073 K before the activity tests using 350 N mL min^{-1} of a 3:1 N_2:H_2 mixture for 4 h. The composition of the product gases was determined by an online connected micro GC equipped with thermal conductivity detector (TCD). The measured parameters were defined as:

$$\text{Methane conversion:} X_{CH4} \ (\%) \ = \ \left(V_{CH4}{}^{in} - V_{CH4}{}^{out}\right)/V_{CH4}{}^{in} \times 100 \tag{1}$$

$$\text{Carbon dioxide conversion:} X_{CO2} \ (\%) \ = \ \left(V_{CO2}{}^{in} - V_{CO2}{}^{out}\right)/V_{CO2}{}^{in} \times 100 \tag{2}$$

$$\text{Hydrogen yield:} H_2 \ \text{yield} \ (\%) \ = \ V_{H2}{}^{out}/\left(2 \times V_{CH4}{}^{in} + V_{H2O}{}^{in}\right) \times 100 \tag{3}$$

$$\left(H_2/CO\right)^{out} \text{molar ratio:} \left(H_2/CO\right)^{out} \ = \ \left(V_{H2}/V_{CO}\right)^{out} \tag{4}$$

where V_i^{in} and V_i^{out} correspond to the inlet and outlet volumetric flow rate of reactant i (NmL/min), respectively.

Process	Feed ratios	WHSV (h^{-1})
Dry reforming (DR)	Biogas: CH_4/CO_2 = 1.5	75.0
Steam reforming (SR)	Biogas + water at S/C = 1.0	104.8
	Biogas + water at S/C = 2.0	134.6
Oxidative reforming (OR)	Biogas + air at O/C = 0.25	131.8
	Biogas + air at O/C = 0.50	188.6
Tri-reforming (TR)	Biogas + water + air at S/C = 1.0 and O/C = 0.25	161.5

Table 5. Summary of the processes and feed ratios for the tests for zeolite L supported catalysts.

The experimental results, summarized in **Figures 9** and **10**, showed that even if in some cases there were no important differences in the hydrogen yield produced by monometallic or bimetallic catalysts, the highest hydrogen yields were generally achieved by bimetallic catalysts.

During DR experiments (**Figure 9(a)**), high conversions and hydrogen yields were achieved. In those conditions, CL (1–3 μm) supported catalysts were the less active ones. On the contrary, Ni/DL catalyst achieved a CH_4 conversion (X CH_4) and consequently hydrogen yield, much higher than equilibrium values, probably caused by the presence of hot spots inside the reactor [12].
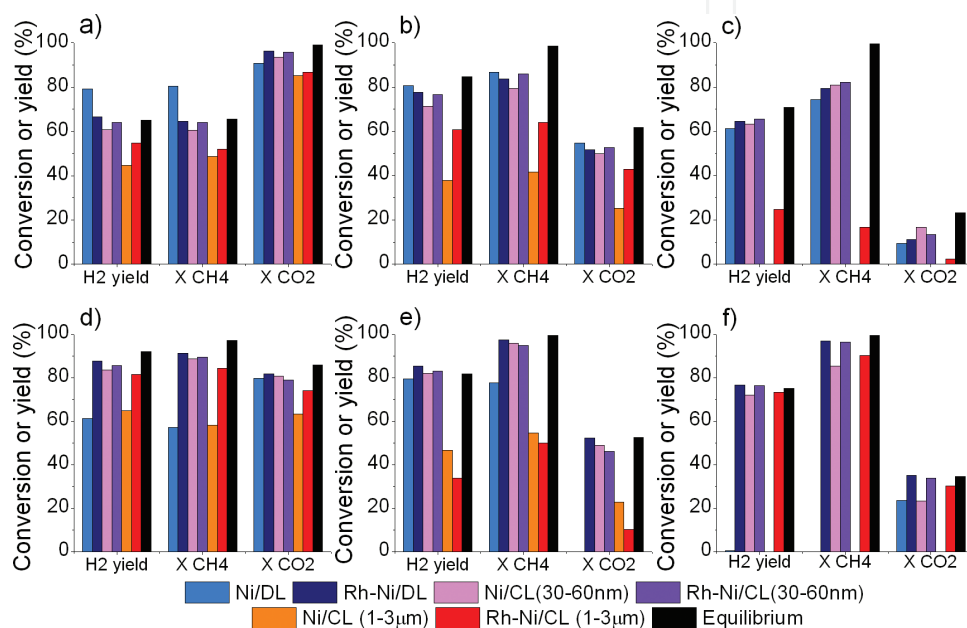

Figure 9. Activity results obtained for several biogas reforming processes carried out at 1073 K and atmospheric pressure at different feeding ratios: (a) DR, (b) SR at S/C = 1.0, (c) SR at S/C = 2.0, (d) OR at O/C = 0.25, (e) OR at O/C = 0.50, and (f) TR at S/C = 1.0 and O/C = 0.25. Figure modified from [12].
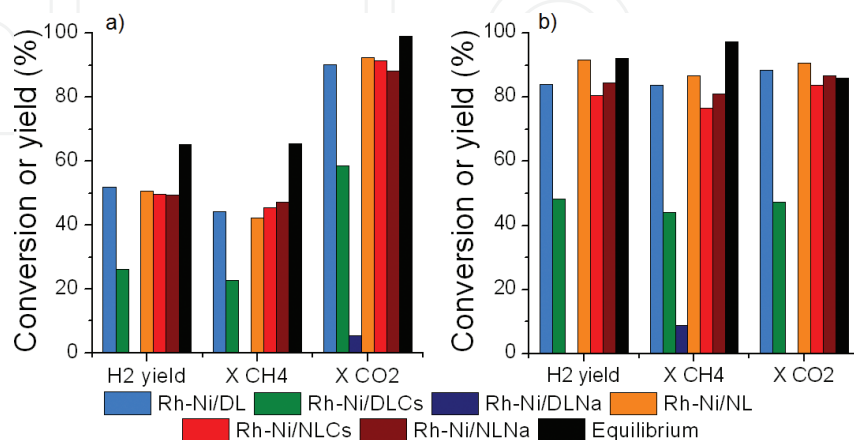

Figure 10. Activity results obtained for two biogas reforming processes at 1073 K and atmospheric pressure: (a) DR and (b) OR at O/C = 0.25. Figure modified from [23].

The addition of steam for SR produced an increase in the methane conversion, but a decrease in the CO_2 conversion (X CO_2) at S/C = 1.0 (**Figure 9(b)**) Thus, the hydrogen yields were higher than in DR conditions for most of the catalysts. However, when the S/C ratio was increased from 1.0 to 2.0 (**Figure 9(c)**) the methane conversion was not increased, but reduced in most of the cases, while the CO_2 conversion was even more reduced. Accordingly, hydrogen yields were also lower when an S/C ratio of 2.0 was used. In both SR experiments, the CL (1–3 μm) supported catalysts achieved again the lowest hydrogen yields because of their low methane conversions. At the S/C ratio of 2.0, the Ni/CL (1–3 μm) catalyst produced a negative CO_2 conversion, due to a higher selectivity to the water gas shift reaction. The rest of the catalysts achieved hydrogen yields, and methane and carbon dioxide conversion values, close to the ones predicted by the equilibrium calculations.

The setting of OR conditions produced some modifications on the activities. When an O/C ratio of 0.25 was used (**Figure 9(d)**), Ni/DL and Ni/CL (1–3 μm) catalysts were the less active ones converting CH_4. Accordingly, they were less active than the rest of the catalysts producing hydrogen. Surprisingly, the Rh-Ni/CL (1–3 μm) catalyst showed similar activities than Rh-Ni/DL, Ni/CL (30–60 nm) and Rh-Ni/CL (30–60 nm) catalysts, with a hydrogen yields, methane and carbon dioxide conversion values above 80%.

Nevertheless, the feeding of a higher amount of oxygen (air) to the reactor (**Figure 9(e)**), demonstrated again the poor activity of the CL (1–3 μm) supported monometallic and bimetallic catalysts in comparison with the rest of the catalysts. Ni/DL catalyst almost produced as much hydrogen as the three most active catalysts. The O/C increase produced an increase of the methane conversion, but a significant decrease in both equilibrium and experimental CO_2 conversion values. The higher CO_2 conversion values measured in OR at O/C = 0.25 than 0.50 could be originated by the lower amount of oxygen available to react with methane (assuming that all the oxygen fed reacts with methane), and therefore, a higher amount of methane is available to react with carbon dioxide by means of the DR reaction.

Finally, when oxygen (air) and steam were fed together with biogas in order to carry out TR experiments (**Figure 9(f)**), results similar to the ones achieved during OR at O/C ratio of 0.25 were obtained. Once again, Ni/DL and Ni/CL (1–3 μm) catalysts were the less active. Surprisingly, the Ni/DL catalyst produced negative CH_4 and CO_2 conversions, thus a methanation reaction was carried out [39]. Ni/CL (1–3 μm) catalyst also produced a negative CO_2 conversion.

Monometallic and bimetallic DL and CL (30–60 nm) supported catalysts achieved the highest methane conversions in most of the studied processes. For those catalysts, the rhodium incorporation improved the methane conversion by reaching values higher than 80%. The methane conversion measured for these two bimetallic catalysts was almost complete when they were tested under OR at O/C = 0.50 and TR conditions. Therefore, the bimetallic catalysts supported on DL and CL (30–60 nm) turned out to be the most appropriates ones for the studied reforming processes. The highest hydrogen yields for the most active catalysts were achieved under OR conditions at the O/C ratio of 0.25.

Due to the poor methane and carbon dioxide conversions reached by Ni and Rh-Ni/CL (1–3 μm) catalysts, their hydrogen production yield was lower than the rest of the catalysts.

For all the experiments, the synthesis gas ratio (H_2/CO molar ratio), was also measured. For liquid hydrocarbon production through Fischer-Tropsch for methanol synthesis, a syngas with a ratio close to 2 is desired. On the other hand, a synthesis gas with a ratio of 1 is necessary for oxo or hydroformylation reaction. According to equilibrium calculations, the SR process at S/C = 2.0 is the only process able to produce a syngas ratio higher than 2. The SR at S/C = 1.0 and TR processes can also produce syngas ratios with values close to 2. Therefore, those processes would require an additional step (apart from the purification) for reaching the desired syngas ratio. On the contrary, for obtaining a syngas ratio close to 1, the equilibrium calculations indicate that both OR processes (at O/C = 0.25 and 0.50) and DR process are more suitable. These equilibrium predicted values were, in general, in good agreement with experimental values for most of the catalysts.

According to the above summarized results, we decided to prepare bimetallic catalysts to study the effect of alkali metals modification. The processes selected to test the bimetallic catalysts were DR and OR (**Figure 10**). On the one hand, the DR process presents the harsher reaction conditions and therefore, it is appropriate to distinguish the activity of the catalysts. On the other hand, the OR process is the most favorable in terms of hydrogen production.

Similar catalytic activity was observed for both studied processes. First, the NL, NLCs, NLNa, and DL supported bimetallic catalysts achieved the highest CH_4 and CO_2 conversions and H_2 yield values, while Ni/DLCs catalyst produced intermediate results. Second, the less active catalyst was Rh-Ni/DLNa, which remained almost inactive in both biogas reforming processes. Therefore, there was a good agreement between the activity, the BET areas, the particle sizes estimated by XRD, and the ones observed by TEM, and the atomic Rh and Ni concentration. Thus, the most active catalysts presented the highest BET areas, the smaller metal particle sizes and the most equilibrated Rh and Ni surface concentrations.

5. Conclusions

The herein reported step-by-step strategy to develop dye- and metal-doped LTL zeolites is suitable to attain materials which can be applied in photonics and eco-friendly catalysis. To this aim, we started from the beginning, by the microwave-assisted synthesis of the LTL zeolite crystals. This kind of heat allows a fine control of the size (from tens of nm to few µm) and shape (from barrels to coins) of the zeolite, which can be tuned just fixing the hydrothermal synthesis conditions. Afterwards, the kind of guest adsorbed into the zeolitic support will rule the application field of the material. On one hand, the allocation of rationally selected fluorophores into the uni-dimensional zeolitic channels, or grafted to the pore entrances, provide a hierarchically ordered material able to harvest light over a broad spectral interval and provide predominant red fluorescence, or alternatively white-light emission, just adjusting the energy transfer efficiency. On the other hand, the deposition of suitable metals onto the zeolite guest boosts the catalysis efficiency in the biogas reforming. Among the different LTL zeolite morphologies used, DL and CL (30–60 nm) supports were the most active ones for the studied reforming processes, especially when Rh and Ni metals were incorporated in order to prepare bimetallic catalysts. High activities are attributed to the high metal dispersion and the strong interactions among NiO and the different supports. The metal exchange of Cs and Na carried out on DL and NL supports mainly affected the morphology, and consequently,

the activity of DL catalyst series. However, the modification of the zeolites with Cs or Na was unsuccessful for biogas reforming catalytic applications because the Rh-Ni/DL and Rh-Ni/NL catalysts showed higher reforming capacity.

Summing up, LTL zeolite arises as a suitable and versatile support to allocate small-enough chromophores into their channels. Such cage effect protects and aligns the fluorophores, whereas the encapsulation enhances the energy transfer efficiency even at low dye loadings, being ideal for antenna or microlaser devices. Besides, its high specific surface allows the incorporation of metals boosting their catalytic efficiency toward the desired reaction, in this case biogas reforming, a long seeking clean energy source as an alternative to polluting fuels.

Acknowledgements

Author details

Leire Gartzia Rivero[1], Jorge Bañuelos[1]*, Kepa Bizkarra[2], Urko Izquierdo[2], Victoria Laura Barrio[2], Jose Francisco Cambra[2] and Iñigo López Arbeloa[1]

*Address all correspondence to: jorge.banuelos@ehu.es

1 Department of Physical Chemistry, University of the Basque Country (UPV/EHU), Bilbao, Spain

2 Faculty of Engineering, University of the Basque Country (UPV/EHU), Bilbao, Spain

References

[1] Ogawa M, Kuroda K. Photofunctions of interaction compounds. Chemical Reviews. 1995;**95**:399-438. DOI: 10.1021/cr00034a005

[2] Cheetman AK, Férey G, Loiseau T. Open-framework inorganic materials. Angewandte Chemie, International Edition. 1999;**38**:3268-3292. DOI: 10.1002/(SICI)1521-3773(19991115) 38:22<3268::AID-ANIE3268>3.0.CO;2-U

[3] Ramamurthy V. Controlling photochemical reactions via confinement: Zeolites. Journal of Photochemistry and Photobiology C. 2000;**1**:145-166. DOI: 10.1016/S1389-5567(00) 00010-1

[4] Tao Y, Kanoh H, Abrams L, Kaneko K. Mesopore-modifed zeolites: Preparation, characterization and applications. Chemical Reviews. 2006;**106**:896-910. DOI: 10.1021/cr040204o

[5] Schulz-Ekloff G, Wöhrle D, van Duffel B, Schoonheydt RA. Chromophores in porous silicas and minerals: Preparation and optical properties. Microporous and Mesoporous Materials. 2002;**51**:91-138. DOI: 10.1016/S1387-1811(01)00455-3

[6] Cronsted AF. Akad. Hankl. Stockholm. 1756;**18**:120. Translation: Sumelius IrG. In: Occelli ML, Robson H. Molecular Sieves. New York: Van Nostrand Reinhold; 1992

[7] Baerlocher C, Meier WH, Olson DH. Atlas of Zeolite Framework Types. 6th ed. Elsevier; 2007. Available from: http://www.iza-structure.org/databases/

[8] Corma A. Inorganic solid acids and their use in acid-catalyzed hydrocarbon reactions. Chemical Reviews. 1995;**95**:559-614. DOI: 10.1021/cr00035a006

[9] Mech A, Monguzzi A, Meinardi F, Mezyk J, Macchi G, Tubino R. Sensitized NIR erbium(III) emission in confined geometries: A new strategy for light emitters in telecom applications. Journal of the American Chemical Society. 2010;**132**:4574-4576. DOI: 10.1021/ja907927s

[10] Devaux A, Calzaferri G, Belser P, Cao P, Brühwiler D, Kunzmann A. Efficient and robust host-guest antenna composite for light harvesting. Chemistry of Materials. 2014;**26**:6878-6885. DOI: 10.1021/cm503761q

[11] Lee TP, Saad B, Ng EP, Salleh B. Zeolite Linde Type L as micro-solid phase extraction sorbent for the high performance liquid chromatography determination of ochratoxin A in coffee and cereal. Journal of Chromatography. A. 2012;**1237**:46-54. DOI: 10.1016/j.chroma.2012.03.031

[12] Izquierdo U, Barrio VL, Bizkarra K, Gutierrez AM, Arraibi JR, Gartzia L, Bañuelos J, Lopez-Arbeloa I, Cambra JF. Ni and Rh-Ni catalysts supported on zeolites L for hydrogen and syngas production by biogas reforming processes. Chemical Engineering Journal. 2014;**238**:178-188. DOI: 10.1016/j.cej.2013.08.093

[13] Gartzia-Rivero L, Bañuelos J, López-Arbeloa I. Photoactive nanomaterials inspired by nature: LTL zeolite doped with laser dyes as artificial light harvesting systems. Materials. 2017;**10**:495. DOI: 10.3390/ma10050495

[14] Huber S, Calzaferri G. Energy transfer from dye-zeolite L antenna crystal to bulk silicon. Chemphyschem. 2004;**5**:239-242. DOI: 10.1002/cphc.200301002

[15] Suarez S, Devaux A, Bañuelos J, Bossart O, Kunzmann A, Calzaferri G. Transparent zeolite-polymer hybrid materials with adaptable properties. Advanced Functional Materials. 2007;**17**:2298-2306. DOI: 10.1002/adfm.200600925

[16] Vohra V, Calzaferri G, Destri S, Pasini M, Porzio W, Botta C. Toward white light emission through efficient two-step energy transfer in hybrid nanofibers. ACS Nano. 2010;**4**:1409-1416. DOI: 10.1021/nn9017922

[17] Vietze U, Kraub O, Laeri F, Ihlein G, Schüth F, Limburg B, Abraham M. Zeolite-dye microlasers. Physical Review Letters. 1998;**81**:4628-4631. DOI: 10.1103/PhysRevLett.81.4628

[18] Marega R, Prasetyanto EA, Michiels C, De Cola L, Bonifazi D. Fast targeting and cancer cell uptake of luminescent antibody-nanozeolite bioconjugates. Small. 2016;**12**:5431-5441. DOI: 10.1002/smll.201601447

[19] Zabala A, Brühwiler D, Ban T, Calzaferri G. Synthesis of zeolite L. Tuning size and morphology. Monatschefte für Chemie. 2005;**136**:77-89. DOI: 10.1007/s00706-004-0253-z

[20] Lupulescu AI, Kumar M, Rimer JD. A facile strategy to design zeolite L crystals with tunable morphology and surface architecture. Journal of the American Chemical Society. 2013;**135**:6608-6617. DOI: 10.1021/ja4015277

[21] Tompsett GA, Conner WC, Yngvesson KS. Microwave synthesis of nanoporous materials. Chemphyschem. 2006;**7**:296-319. DOI: 10.1002/cphc.200500449

[22] Bilecka I, Niederberger M. Microwave chemistry for inorganic nanomaterials synthesis. Nanoscale. 2010;**2**:1358-1374. DOI: 10.1039/B9NR00377K

[23] Gartzia-Rivero L, Bañuelos J, Izquierdo U, Barrio VL, Bizkarra K, Cambra JF, López-Arbeloa I. Microwave synthesis of LTL zeolites with tunable size and morphology: An optimal support for metal-catalyzed hydrogen production from biogas reforming processes. Particle and Particle Systems Characterization. 2014;**31**:110-120. DOI: 10.1002/ppsc.201300275

[24] Calzaferri G. Nanochannels: Hosts for the supramolecular organization of molecules and complexes. Langmuir. 2012;**28**:6216-6231. DOI: 10.1021/la3000872

[25] Martínez-Martínez V, García R, Sola-Llano R, Gómez-Hortigüela L, Sola-Lano R, Pérez-Pariente J, López-Arbeloa I. Highly luminescent and optically switchable hybrid material by one-pot encapsulation of dyes into MgAPO-11 unidirectional nanopores. ACS Photonics. 2014;**1**:205-211. DOI: 10.1021/ph4000604

[26] Benniston AC, Harriman A. Artificial photosynthesis. Materials Today. 2008;**11**:26-34. DOI: 10.1016/S1369-7021(08)70250-5

[27] El-Khouly M, El-Mohsnawy E, Fukuzumi S. Solar energy conversion: From natural to artificial photosynthesis. Journal of Photochemistry and Photobiology C. 2017;**31**:36-83. DOI: 10.1016/j.jphotochemrev.2017.02.001

[28] Zan G, Wu Q. Biomimetic and bioinspired synthesis of nanomaterials/nanostructures. Advanced Materials. 2016;**28**:2099-2147. DOI: 10.1002/adma.201503215

[29] Scholes GD, Fleming GR, Olaya-Castro A, van Grondelle R. Lessons from nature about solar light harvesting. Nature Chemistry. 2011;**3**:763-774. DOI: 10.1038/nchem.1145

[30] Hötzer B, Medintz IL, Hildebrandt N. Fluorescence in nanobiotechnology: Sophisticated fluorophores for novel applications. Small. 2012;**8**:2297-2326. DOI: 10.1002/smll.201200109

[31] Claassens NJ, Volpers M, Santos V, van der Oost J, de Vos WM. Potential of proton-pumping rhodopsins: Engineering photosystems into microorganisms. Trends in Biotechnology. 2013;**31**:633-642. DOI: 10.1016/j.tibtech.2013.08.006

[32] Feng X, Ding X, Chen L, Wu Y, Liu L, Addicoat M, Irle S, Dong Y, Jiang D. Two-dimensional artificial light-harvesting antennae with predesigned high-order structure and robust photosensitizing activity. Scientific Reports. 2016;**6**:32944. DOI: 10.1038/srep32944

[33] Insuwan W, Rangsriwatananon K, Meeprasert J, Namuangruk S, Surakhot Y, Kungwan N, Jungsuttiwong S. Combined experimental and theoretical investigation on fluorescence

resonance energy transfer of dye loaded on LTL zeolite. Microporous and Mesoporous Materials. 2017;**241**:372-382. DOI: 10.1016/j.micromeso.2016.12.020

[34] Loudet A, Burgess K. BODIPY dyes and their derivatives: Syntheses and spectroscopic properties. Chemical Reviews. 2007;**107**:4891-4932. DOI: 10.1021/cr078381n

[35] Frontera P, Macario A, Aloise A, Crea F, Antonucci PL, Nagy JB, Frsusteri F, Giordano G. Catalytic dry-reforming on Ni–zeolite supported catalyst. Catalysis Today. 2012;**179**: 52-60. DOI: 10.1016/j.cattod.2011.07.039

[36] Bereketidou OA, Goula MA. Biogas reforming for syngas production over nickel supported on ceria-alumina catalysts. Catalysis Today. 2012;**195**:93-100. DOI: 10.1016/j.cattod.2012.07.006

[37] Damyanova S, Pawelec B, Arishtirova K, Fierro JLG. Biogas reforming over bimetallic PdNi catalysts supported on phosphorus-modified alumina. International Journal of Hydrogen Energy. 2011;**36**:10635-10647. DOI: 10.1016/j.ijhydene.2011.05.098

[38] Xu J, Zhou W, Li Z, Wang J, Ma J. Biogas reforming for hydrogen production over a Ni-Co bimetallic catalyst: Effect of operating conditions. International Journal of Hydrogen Energy. 2010;**35**:13013-13020. DOI: 10.1016/j.ijhydene.2010.04.075

[39] Kaengsilalai A, Luengnaruemitchai A, Jitkarnka S, Wongkasemjit S. Potential of Ni supported on KH zeolite catalysts for carbon dioxide reforming of methane. Journal of Power Sources. 2007;**165**:347-352. DOI: 10.1016/j.jpowsour.2006.12.005

[40] Nimwattanakul W, Luengnaruemitchai A, Jitkarnka S. Potential of Ni supported on clinoptilolite catalysts for carbon dioxide reforming of methane. International Journal of Hydrogen Energy. 2006;**31**:93-100. DOI: 10.1016/j.ijhydene.2005.02.005

[41] San-José-Alonso D, Juan-Juan J, Illán-Gómez MJ, Román-Martínez MC. Ni, Co and bimetallic Ni–Co catalysts for the dry reforming of methane. Applied Catalysis A: General. 2009;**371**:54-59. DOI: 10.1016/j.apcata.2009.09.026

[42] Diskin AM, Cunningham RH, Ormerod RM. The oxidative chemistry of methane over supported nickel catalysts. Catalysis Today. 1998;**46**:147-154

[43] Luengnaruemitchai A, Kaengsilalai A. Activity of different zeolite-supported Ni catalysts for methane reforming with carbon dioxide. Chemical Engineering Journal. 2008;**144**:96-102. DOI: 10.1016/j.cej.2008.05.023

[44] Garrido Pedrosa AM, Souza MJB, Silva AOS, Melo DMA, Araujo AS. Synthesis, characterization and catalytic properties of the cobalt and nickel supported on HZSM-12 zeolite. Catalysis Communications. 2006;**7**:791-796. DOI: 10.1016/j.catcom. 2006.02.012

[45] El Doukkali M, Iriondo A, Cambra JF, Jalowiecki-Duhamel L, Mamede AS, Dumeignil F, Arias PL. Pt monometallic and bimetallic catalysts prepared by acid sol–gel method for liquid phase reforming of bioglycerol. Journal of Molecular Catalysis A: Chemical. 2013;**368-369**:125-136. DOI: 10.1016/j.molcata.2012.12.006

[46] Ocsachoque M, Pompeo F, Gonzalez G. Rh-Ni/CeO_2-Al_2O_3 catalysts for methane dry reforming. Catalysis Today. 2011;**172**:226-231. DOI: 10.1016/j.cattod.2011.02.057